

HADES RV Programme with HARPS-N at TNG

V. A super-Earth on the inner edge of the habitable zone of the nearby M dwarf GJ 625^{★,★★}

A. Suárez Mascareño^{1,2,3}, J. I. González Hernández^{1,3}, R. Rebolo^{1,3,4}, S. Velasco^{1,3}, B. Toledo-Padrón^{1,3}, L. Affer⁵, M. Perger⁶, G. Micela⁵, I. Ribas⁶, J. Maldonado⁵, G. Leto⁷, R. Zanmar Sanchez⁷, G. Scandariato⁷, M. Damasso⁸, A. Sozzetti⁸, M. Esposito⁹, E. Covino⁹, A. Maggio⁵, A. F. Lanza⁷, S. Desidera¹⁰, A. Rosich⁶, A. Bignamini¹¹, R. Claudi¹⁰, S. Benatti¹⁰, F. Borsa¹², M. Pedani¹³, E. Molinari¹³, J. C. Morales⁶, E. Herrero⁶, and M. Lafarga⁶

¹ Instituto de Astrofísica de Canarias, 38205 La Laguna, Tenerife, Spain
e-mail: jonay@iac.es

² Observatoire Astronomique de l'Université de Genève, 1290 Versoix, Switzerland
e-mail: Alejandro.SuarezMascareno@unige.ch

³ Universidad de La Laguna, Dpto. Astrofísica, 38206 La Laguna, Tenerife, Spain

⁴ Consejo Superior de Investigaciones Científicas, 28006 Madrid, Spain

⁵ INAF-Osservatorio Astronomico di Palermo, Piazza del Parlamento 1, 90134 Palermo, Italy

⁶ Institut de Ciències de l'Espai (CSIC-IEEC), Campus UAB, Carrer de Can Magrans s/n, 08193 Cerdanyola del Vallés, Spain

⁷ INAF-Osservatorio Astrofisico di Catania, via S. Sofia 78, 95123 Catania, Italy

⁸ INAF-Osservatorio Astrofisico di Torino, via Osservatorio 20, 10025 Pino Torinese, Italy

⁹ INAF-Osservatorio Astronomico di Capodimonte, via Moiariello, 16, 80131 Napoli, Italy

¹⁰ INAF-Osservatorio Astronomico di Padova, Vicolo dell'Osservatorio 5, 35122 Padova, Italy

¹¹ INAF-Osservatorio Astronomico di Trieste, via Tiepolo 11, 34143 Trieste, Italy

¹² INAF-Osservatorio Astronomico di Brera, via E. Bianchi 46, 23807 Merate (LC), Italy

¹³ Fundación Galileo Galilei, INAF, Rambla José Ana Fernández Pérez 7, 38712 Breña Baja, TF, Spain

Received 7 April 2017 / Accepted 16 May 2017

ABSTRACT

We report the discovery of a super-Earth orbiting at the inner edge of the habitable zone of the star GJ 625 based on the analysis of the radial-velocity (RV) time series from the HARPS-N spectrograph, consisting of 151 HARPS-N measurements taken over 3.5 yr. GJ 625 b is a planet with a minimum mass $M \sin i$ of $2.82 \pm 0.51 M_{\oplus}$ with an orbital period of 14.628 ± 0.013 days at a distance of 0.078 AU from its parent star. The host star is the quiet M2 V star GJ 625, located at 6.5 pc from the Sun. We find the presence of a second radial-velocity signal in the range 74–85 days that we relate to stellar rotation after analysing the time series of Ca II H&K and H α spectroscopic indicators, the variations of the FWHM of the CCF, and the APT2 photometric light curves. We find no evidence linking the short-period radial-velocity signal to any activity proxy.

Key words. planetary systems – techniques: radial velocities – stars: activity – stars: chromospheres – stars: individual: GJ 625 – planets and satellites: detection

1. Introduction

The detection rate of potentially habitable Earth-like planets around M dwarfs is rapidly increasing (Wright et al. 2016; Anglada-Escudé et al. 2016; Jehin et al. 2016; Gillon et al. 2017; Astudillo-Defru et al. 2017). For many years it has been

* Based on observations made with the Italian Telescopio Nazionale Galileo (TNG), operated on the island of La Palma by the INAF – Fundación Galileo Galilei at the Roche de Los Muchachos Observatory of the Instituto de Astrofísica de Canarias (IAC); photometric observations made with the robotic telescope APT2 (within the EXORAP programme) located at Serra La Nave on Mt. Etna; and lucky imaging observations made with the Telescopio Carlos Sánchez operated on the island of Tenerife by the Instituto de Astrofísica de Canarias in the Spanish Observatorio del Teide.

** Tables A.1–A.5 are only available at the CDS via anonymous ftp to cdsarc.u-strasbg.fr (130.79.128.5) or via <http://cdsarc.u-strasbg.fr/viz-bin/qcat?J/A+A/605/A92>

clear that M dwarfs are a shortcut to finding earth-like planets and therefore several surveys have attempted to take advantage of their low masses and closer habitable zones (Quirrenbach et al. 2012; Bonfils et al. 2013; Howard et al. 2014; Irwin et al. 2015; Berta-Thompson et al. 2015; Affer et al. 2016; Suárez Mascareño et al. 2017a; Perger et al. 2017b). M dwarfs have also proven to be difficult targets because of their stellar activity. The signals induced by the stellar rotation can easily mimic those of planetary origin (Queloz et al. 2001; Bonfils et al. 2007; Boisse et al. 2011; Robertson et al. 2014; Suárez Mascareño et al. 2015, 2017a,b; Newton et al. 2016; Vanderburg et al. 2016). For the case of M dwarfs, these signals tend to be comparable to those of rocky planets close to the habitable zone of their stars (Howard et al. 2014; Robertson et al. 2014; Suárez Mascareño et al. 2015, 2017b; Newton et al. 2016). The interpretation of the radial-velocity curves of M dwarfs is usually complicated even in the quietest

of stars. Low mass stars are the most common type of stars; they offer valuable complementary information on the formation mechanisms of planetary systems. For instance, giant planets at close orbits are known to be rare around M dwarfs (Endl et al. 2006), while low mass rocky planets appear to be more frequent (Bonfils et al. 2013; Dressing & Charbonneau 2013; Dressing et al. 2015).

Even with the large number of confirmed exoplanets (Howard et al. 2009, 2012; Mayor et al. 2011) the number of rocky planets remains comparably small with only about a hundred known around M dwarfs. This is mostly because most surveys – including the *Kepler* survey – have focused primarily on solar-type and K-type stars. In recent years many planetary systems hosting Neptune mass planets and super-Earths have been reported (Udry et al. 2007; Delfosse et al. 2013; Howard et al. 2014; Astudillo-Defru et al. 2015), and a rapidly increasing number of Earth-mass planets as well (Mayor et al. 2009; Berta-Thompson et al. 2015; Wright et al. 2016; Affer et al. 2016; Anglada-Escudé et al. 2016; Jehin et al. 2016; Suárez Mascareño et al. 2017a; Gillon et al. 2017). However, the frequency of Earth-sized planets around M dwarfs is still not well established. Several studies have attempted to quantify the abundance of rocky planets in close orbits and in the habitable zones of M dwarfs, but the uncertainties are still large, making it important to continue adding new planets to the sample (Bonfils et al. 2013; Gaidos 2013; Kopparapu 2013).

We report the discovery of a super-Earth orbiting the nearby star GJ 625 on the inner edge of its habitable zone. The discovery is part of the HADES (HARPS-n red Dwarf Exoplanet Survey) radial velocity (RV) programme with HARPS-N at the Telescopio Nazionale *Galileo* in La Palma (Spain). The HADES RV programme is the result of a collaborative effort between the Italian Global Architecture of Planetary Systems (GAPS, Covino et al. 2013; Poretti et al. 2016) Consortium, The Institut de Ciències de l’Espai de Catalunya (ICE), and the Instituto de Astrofísica de Canarias (IAC). The HADES team has previously discovered two super-Earth exoplanets of minimum masses of ~ 6.3 and $\sim 2.5 M_{\oplus}$ orbiting the early-type M dwarf GJ 3998 (Affer et al. 2016).

GJ 625 is a bright ($V = 10.17$ mag) low activity ($\log_{10}(R'_{\text{HK}}) \sim -5.5$) M dwarf located at a distance of 6.5 pc from the Sun (van Leeuwen 2007; Gaia Collaboration 2016). Table 1 shows the stellar parameters. Its low activity combined with its long rotation period of more than 70 days makes it a very interesting candidate to search for rocky planets.

2. Data and observations

2.1. Spectroscopy

The star GJ 625 is part of the HADES RV programme (Affer et al. 2016) and has been extensively monitored since 2013. We used 151 HARPS-N spectra taken over 3.5 yr. HARPS-N (Cosentino et al. 2012) is a fibre-fed high resolution echelle spectrograph installed at the Telescopio Nazionale *Galileo* in the Roque de los Muchachos Observatory (Spain). The instrument has a resolving power greater than $R \sim 115\,000$ over a spectral range from ~ 380 to ~ 690 nm and has been designed to attain very high long-term radial-velocity precision. It is contained in a vacuum vessel to avoid spectral drifts due to temperature and air pressure variations, thus ensuring its stability. HARPS-N is equipped with its own pipeline providing extracted and wavelength-calibrated spectra, as well as RV

Table 1. Stellar parameters of GJ 625.

Parameter	GJ 625	Ref.
RA (J2000)	16:25:25.36	1
Dec (J2000)	+54:18:12.19	1
μ_{α} (mas yr $^{-1}$)	432.13	1
μ_{δ} (mas yr $^{-1}$)	-171.48	1
Distance [pc]	6.49	1
m_B	11.80 ± 0.16	2
m_V	10.17 ± 0.04	2
Spectral Type	M2	3
T_{eff} [K]	3499 ± 68	3
[Fe/H]	-0.38 ± 0.09	3
M_{\star} [M_{\odot}]	0.30 ± 0.07	3
R_{\star} [R_{\odot}]	0.31 ± 0.06	3
$\log g$ (cgs)	4.94 ± 0.06	3
$\log(L_{\star}/L_{\odot})$	-1.894 ± 0.170	3
$\log_{10}(R'_{\text{HK}})$	-5.5 ± 0.2	0
P_{rot} (days)	77.8 ± 5.5	0
$v \sin i$ (km s $^{-1}$)	$<0.2^*$	3
Secular acc. (m s $^{-1}$ yr $^{-1}$)	0.03	4

Notes. (*) Calculated using the radius estimated by Maldonado et al. (2017) and our period determination.

References. (0) – This work; (1) – Gaia Collaboration (2016); (2) – Høg et al. (2000); (3) – Maldonado et al. (2017); (4) – Calculated following Montet et al. (2014).

measurements and other data products such as cross-correlation functions (CCF) and their bisector profiles.

Most of the observations were carried out using the Fabry Perot (FP) interferometer for simultaneous calibration. The FP offers the possibility of monitoring the instrumental drift with a precision of 10 cm s $^{-1}$ without the risk of contamination of the stellar spectra by the ThAr saturated lines (Wildi et al. 2010). While this is not usually a problem in G and K stars, the small amount of light collected in the blue part of the spectra of M dwarfs might compromise the quality of the measurement of the Ca II H&K flux. The FP allows a precision of ~ 1 m s $^{-1}$ in the determination of the radial velocities of the spectra with the highest signal-to-noise ratios while assuring the quality of the spectroscopic indicators even in those spectra with low signal-to-noise ratios. Those observations taken without the FP were taken without simultaneous lamp reference.

2.2. EXORAP photometry

Along with the HARPS-N spectra we have 2.6 yr of B , V , R , and I -band photometric data collected at the INAF-Catania Astrophysical Observatory with an 80 cm f/8 Ritchey-Chretien robotic telescope (APT2) located at Serra la Nave on the Mt. Etna. The data is reduced by overscan, bias, dark subtraction, and flat fielding with IRAF¹ procedures and visually inspected to check the quality (see Affer et al. 2016 for details). Errors in the individual measurements are the quadratic sum of the intrinsic noise (photon noise and sky noise) and the RMS of the ensemble stars used for the differential photometry.

¹ IRAF is distributed by the National Optical Astronomy Observatories, which are operated by the Association of Universities for Research in Astronomy, Inc., under cooperative agreement with the National Science Foundation.

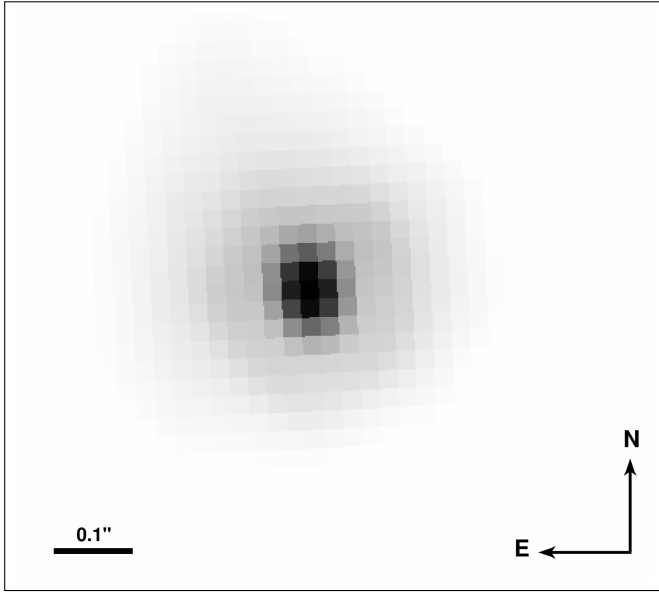


Fig. 1. Diffraction-limited image of GJ 625 after lucky imaging processing with a selection of the 30% best individual TCS/FastCam frames.

2.3. FastCam lucky imaging observations

On June 6, 2016, we collected 50 000 individual frames of GJ 625 in the *I* band using the lucky imaging FastCam instrument (Oscz et al. 2008) at the 1.5 m Carlos Sánchez Telescope in the Observatorio del Teide, Tenerife, with 30 ms exposure time for each frame. FastCam is an optical imager with a low noise EMCCD camera which allows to obtain speckle-featuring not saturated images at a fast frame rate (Labadie et al. 2011).

In order to construct a high resolution, diffraction limited, long-exposure image, the individual frames were bias subtracted, aligned, and co-added using our own lucky imaging algorithm (Velasco et al. 2016). Figure 1 presents the high resolution image constructed by co-addition of the best percentage of the images using lucky imaging and shift-and-add algorithms. Owing to the atmospheric conditions of the night, the selection of 30% of the individual frames was found to be the best solution to produce a deep and diffraction limited image of the target, resulting in a total integration time of 450 s. The combined image achieved $\Delta m_I = 4.5\text{--}5.0$ at $1''$. We find no bright contaminant star in the diffraction limited image.

3. Determination of stellar activity indicators and radial velocities

3.1. Activity indicators

For the activity analysis we use the extracted order-by-order wavelength-calibrated spectra produced by the HARPS-N pipeline. For a given star, the change in atmospheric transparency from day to day causes variations in the flux distribution of the recorded spectra that are particularly relevant in the blue, where we intend to measure Ca II lines. In order to minimize the effects related to these atmospheric changes we create a spectral template for each star by de-blazing and co-adding every available spectrum, and use the co-added spectrum to correct the order-by-order fluxes of the individual ones. We also correct each spectrum for the Earth's barycentric radial velocity and the radial velocity of the star using the measurements

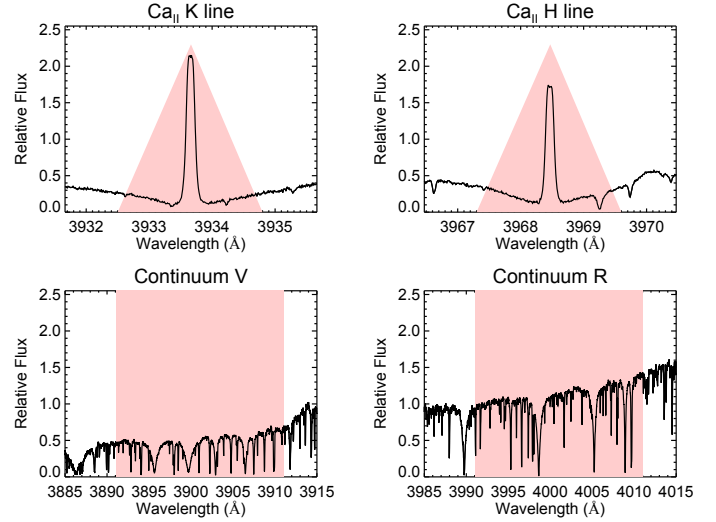


Fig. 2. Ca II H&K filter of the spectrum of the star GJ 625 with the same shape as the Mount Wilson Ca II H&K passband.

given by the standard pipeline, and re-binned the spectra into a wavelength-constant step. Using this HARPS-N dataset, we expect to have high quality spectroscopic indicators to monitor tiny stellar activity variations with high accuracy.

S_{MW} index

We calculate the Mount Wilson S index and the $\log_{10}(R'_{HK})$ by using the original Noyes et al. (1984) procedure, following Lovis et al. (2011) and Suárez Mascareño et al. (2015, 2017a). We define two triangular-shaped passbands with full width half maximum (FWHM) of 1.09 \AA centred at 3968.470 \AA and 3933.664 \AA for the Ca II H&K line cores, and for the continuum we use two bands 20 \AA in width centred at 3901.070 \AA (V) and 4001.070 \AA (R), as shown in Fig. 2.

Then the S -index is defined as

$$S = \alpha \frac{\tilde{N}_H + \tilde{N}_K}{\tilde{N}_R + \tilde{N}_V} + \beta, \quad (1)$$

where \tilde{N}_H , \tilde{N}_K , \tilde{N}_R , and \tilde{N}_V are the mean fluxes per wavelength unit in each passband, while α and β are calibration constants fixed as $\alpha = 1.111$ and $\beta = 0.0153$. The S index (S_{MW}) serves as a measurement of the Ca II H&K core flux normalized to the neighbour continuum. As a normalized index for comparison to other stars, we compute the $\log_{10}(R'_{HK})$ following Suárez Mascareño et al. (2015).

$H\alpha$ index

We also use the $H\alpha$ index, with a simpler passband following Gomes da Silva et al. (2011) and Suárez Mascareño et al. (2017a). It consists of a rectangular bandpass with a width of 1.6 \AA and centred at 6562.808 \AA (core), and two continuum bands of 10.75 \AA and 8.75 \AA in width centred at 6550.87 \AA (L) and 6580.31 \AA (R), respectively, as seen in Fig. 3.

Thus, the $H\alpha$ index is defined as

$$H\alpha_{\text{Index}} = \frac{\tilde{H}\alpha_{\text{core}}}{\tilde{H}\alpha_L + \tilde{H}\alpha_R}, \quad (2)$$

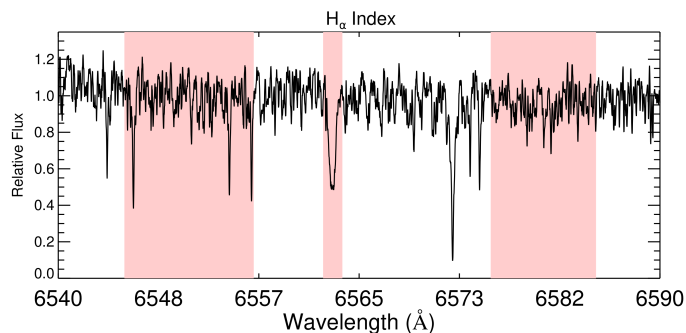


Fig. 3. Spectrum of the M-type star GJ 625 showing the H α region of the spectrum. The light red shaded regions show the filter passband and continuum bands.

where $\bar{H}\alpha_{\text{core}}$, $\bar{H}\alpha_L$, and $\bar{H}\alpha_R$ are the mean fluxes per wavelength unit in each of the previously defined passbands.

3.2. Radial velocities

The radial-velocity measurement in the HARPS-N standard pipeline is determined by a Gaussian fit of the CCF of the spectrum with a synthetic stellar template (Baranne et al. 1996; Pepe et al. 2000) that consists of a series of delta functions at the positions of isolated stellar lines at wavelengths longer than 4400 Å. In the case of M dwarfs, due to the huge number of line blends, the CCF is not Gaussian, resulting in a less precise Gaussian fit which might cause distortions in the radial-velocity measurements and decrease the sensibility in the measurement of the variations in the full width half maximum (FWHM) of the CCF. To deal with this issue we tried two different approaches, as in Suárez Mascareño et al. (2017a).

The first approach consisted in using a slightly more complex model for the CCF fitting, a Gaussian function plus a second-order polynomial using only the central region of the CCF function. We use a 15 km s⁻¹ window centred at the minimum of the CCF. This configuration provides the best stability of the measurements. Along with the measurements of the radial velocity, we obtain the FWHM of the CCF which we also use to track variations in the activity level of the star. A second approach to the problem was to recompute the radial velocities using the TERRA pipeline (Anglada-Escudé & Butler 2012), which is a template-matching algorithm with a high signal-to-noise stellar spectral template. Every spectrum is corrected for both barycentric and stellar radial velocity to align it to the frame of the solar system barycentre. The radial velocities are computed by minimizing the χ^2 of the residuals between the observed spectra and shifted versions of the stellar template, where all the elements contaminated by telluric lines are masked. In this case we use the Doppler information at wavelengths longer than 4550 Å. All radial-velocity measurements are corrected from the secular acceleration of the star.

For the bisector span measurement we rely on the pipeline results as it does not depend on the fit but on the CCF itself. The bisector has been a standard activity diagnostic tool for solar-type stars for over 10 yr. Unfortunately, its behaviour in slow rotating stars is not as informative as it is for fast rotators (Saar & Donahue 1997; Bonfils et al. 2007). We report the measurements of the bisector span (BIS) for each radial-velocity measurement, but we do not find any meaningful information in its analysis.

3.3. Quality control of the data

As the sampling rate of our data is not well suited for modelling fast events like flares, and their effect on the radial velocity is not well understood, we identify and reject points likely affected by flares by searching for an abnormal behaviour of the activity indicators (Reiners 2009). The process rejected 11 spectra that correspond to flare events of the star with obvious activity enhancement and line distortion, which leaves us with 140 HARPS-N spectroscopic observations taken over 3.3 yr with a typical exposure of 900 s and an average signal-to-noise ratio of 56 at 5500 Å. All measurements and their uncertainties are listed in Table A.1.

4. Analysis

In order to properly understand the behaviour of the star, our first step is to analyse the different modulations present in the photometric and spectroscopic time series.

We search for periodic variability compatible with both stellar rotation and long-term magnetic cycles. We compute the power spectrum using a generalized Lomb-Scargle periodogram (Zechmeister & Kürster 2009) and if there is any significant periodicity we fit the detected period using a sinusoidal model or a double harmonic sinusoidal model to account for the asymmetry of some signals (Berdyugina & Järvinen 2005) with the MPFIT routine (Markwardt 2009). The model used for the preliminary analysis is chosen based on the reduced χ^2 of the fit.

The significance of the periodogram peak was evaluated using both the Cumming (2004) modification of the Horne & Baliunas (1986) formula to obtain the spectral density thresholds for a desired false alarm probability (FAP) level and the bootstrap randomization (Endl et al. 2001) of the data. We finally opted for the power spectral density (PSD) levels given by the bootstrap process because they were the most conservative.

Radial velocities. For the analysis of the radial velocities we use the measurements given by the CCF and by the TERRA pipeline. We have 140 measurements distributed over 3.3 yr. The star shows a mean RV of -12.850 km s⁻¹. The CCF RV measurements show an RMS of 2.56 m s⁻¹ with a typical uncertainty of 1.32 m s⁻¹, while the TERRA RV measurements show an RMS of 2.57 m s⁻¹ with a typical uncertainty of 1.24 m s⁻¹. Figure 4 shows both time series of RVs. The two sets show a very similar scatter, but the TERRA data have slightly smaller error bars.

We find a clear dominant signal in the data in both series with a FAP < 0.1% (although more significant in the TERRA data). The signal has a period of 14.629 ± 0.069 days in the CCF series and 14.629 ± 0.077 days in the TERRA series, a semi-amplitude of 1.85 ± 0.13 m s⁻¹ in the CCF data, and a semi-amplitude of 1.65 ± 0.18 m s⁻¹ in the TERRA data. Figure 5 shows the combined periodograms of the two data series, and Fig. 6 shows the phase-folded fits of both series. When analysing the residuals we see a structure of different signals between ~ 65 and ~ 100 days (see Fig. 5). Of these signals, the most significant one is not the same in the CCF and TERRA data. The CCF data shows a 74.7 ± 1.9 d signal with a semi-amplitude of 1.64 ± 0.18 m s⁻¹, while the TERRA data shows a 85.9 ± 2.8 d signal with a semi-amplitude of 1.58 ± 0.18 m s⁻¹. Figure 7 shows the phase-folded curves for those signals. No other significant signals are found in the RV data. The RMS of the remaining residuals is 2.0 m s⁻¹ in both cases.

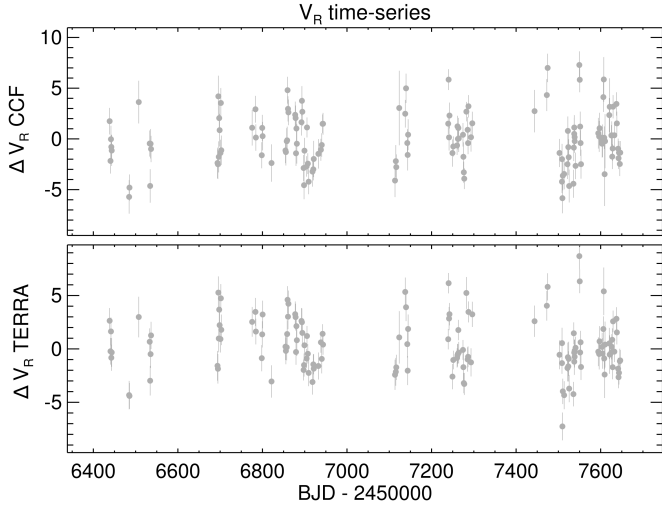


Fig. 4. Radial-velocity time series for the CCF RVs (*top panel*) and the TERRA RVs (*bottom panel*).

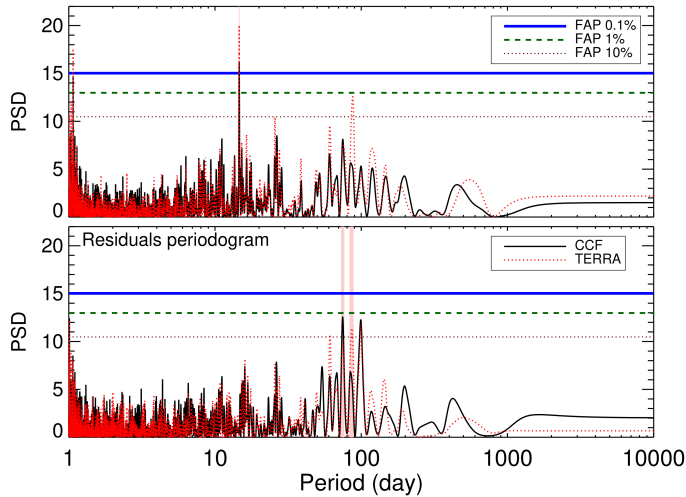


Fig. 5. Periodograms of the radial-velocity time series. *Top panel*: periodogram of the raw RVs for the CCF (black line) and the TERRA (red dotted line). *Bottom panel*: periodogram of the residuals for both the CCF (black line) and TERRA (red dotted line). The light red shaded regions show the detected periodicities.

Spectroscopic indicators. Figure 8 shows the time series for the four spectroscopic indicators used for the activity analysis: S_{MW} index, H_α index, FWHM, and bisector span time series. For the four quantities we have 140 measurements distributed over 3.3 yrs. For the S_{MW} index data we measure a mean value of 0.735 (corresponding to a $\log_{10}(R'_{HK})$ of -5.5) with an RMS of the data of 0.094 and a typical uncertainty of the individual measurement of 0.012. Using the activity relationships of Suárez Mascareño et al. (2015, 2016) we come to expect a rotation period of around 80 ± 20 days. For the H_α index we measure a mean value of 0.41607 with an RMS of the data of 0.00729 and a typical uncertainty of 0.00070. For the case of the FWHM time series we measure a mean FWHM of 3.83 km s^{-1} with an RMS of the data of 5.32 m s^{-1} and a typical uncertainty of 2.0 m s^{-1} . For the bisector span we measure a mean span of -6.72 m s^{-1} with an RMS of the data of 2.28 m s^{-1} and a typical uncertainty of 2.0 m s^{-1} .

Figure 9 shows the periodograms for the four spectroscopic indicators. We see an indication of a long-term signal in the S_{MW} and H_α indexes. In the S_{MW} index periodogram it appears as a double peak at ~ 1.7 yr and ~ 3.2 yr, with large uncertainties in both cases. In the H_α index periodogram there is a single peak at ~ 3.4 yr. These signals would be compatible with short magnetic cycles, either flip-flop or global cycles (Berdyugina & Usoskin 2003; Moss 2004; Suárez Mascareño et al. 2016). The longer period peaks in both indexes seem to be the mark of the same ~ 3.4 yr signal, while the shorter period peak in the S_{MW} index might be an artefact caused by the extremely asymmetric signal. It might also be a flip-flop cycle combined with a 3.4 yr global cycle. More observations will be needed to confirm and constrain the cycle length and nature. Our 3.3 yr baseline of observations is too short to reach a unique conclusion on the nature of these long-term signals. In addition to the long-term signals, three shorter period signals appear in the S_{MW} , H_α , and FWHM time series of 74, 85, and 82 days, respectively. These signals are consistent with the expected rotation period of the star. The S_{MW} index signal is a 73.7 ± 2.2 d signal with a semi-amplitude of 0.0413 ± 0.0020 detected with a FAP $< 1\%$. The signal in the H_α index is a 85.2 ± 2.2 d signal with a semi-amplitude of 0.00217 ± 0.00014 detected with a FAP $< 10\%$. Finally the FWHM signal has a period of 82.0 ± 3.1 days, a semi-amplitude $4.03 \pm 0.38 \text{ m s}^{-1}$, and a FAP $< 0.1\%$. Figure 10 shows the phase-folded curves of the three signals.

No other significant signals are found in any of the time series after subtracting these signals.

Photometry. In order to confirm the possible activity-induced signals present in the RV time series and in the time series of spectroscopic indicators we analyse the BVRI photometric time series. Figure 11 and Table 2 show the available data. All the series show the presence of some long-term evolution, which is still not well covered by our observation baseline.

We subtract the long-term evolution using a polynomial fit and analyse the residuals of the fit for periodic signals. Figure 12 shows the periodograms of the time series for the four filters. Several significant signals appear in the periodograms of the different time series, but we find one common periodicity for the m_B , m_V , and m_R series at ~ 74 d. We do not find any significant signal in the m_I series periodogram; the I band is the smallest dataset, so this is not surprising. We find a very significant (FAP $< 0.1\%$) signal at 73.9 ± 3.4 days with a semi-amplitude of 12.1 ± 0.3 mmag in the B -band time series (Fig. 13, left panel), a significant (FAP $< 1\%$) signal at 73.9 ± 3.7 days with a semi-amplitude of 8.2 ± 0.3 mmag in the V -band time series (Fig. 13, middle panel), and a less significant (FAP $< 10\%$) signal at 73.6 ± 2.8 days with a semi-amplitude of 7.8 ± 0.3 mmag for the R -band time series (Fig. 13, right panel). No other significant signals are found in the V - and R -band series after subtracting the detected signals. For the case of the B band there is a remaining signal at ~ 1 yr with a second peak at ~ 0.5 yr which seem to be an artefact.

5. Interpretation of the detected signals

The previous analysis unveiled several signals at different timescales. Some of them are common among different datasets. Table 3 shows the measured signals for the different datasets of GJ 625. We can identify six different signals: at ~ 3 yr, at ~ 1.6 yr, at ~ 85 day, at ~ 82 day, at ~ 74 day, and at ~ 14.6 day.

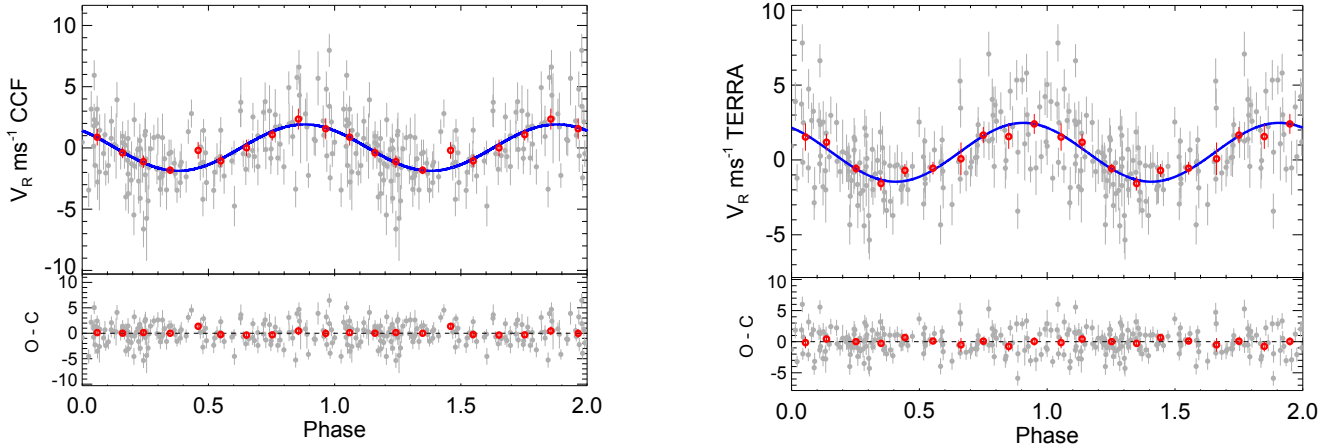


Fig. 6. Phase-folded curve of the raw RV data using the 14.6-day periodicity. *Left panel:* CCF measurements; *right panel:* TERRA measurements. The red dots are the same points binned in phase with a bin size of 0.1. The error bar of a given bin is estimated using the weighted standard deviation of binned measurements divided by the square root of the number of measurements included in this bin. The blue solid line shows the best fit to the data using a sinusoidal fit.

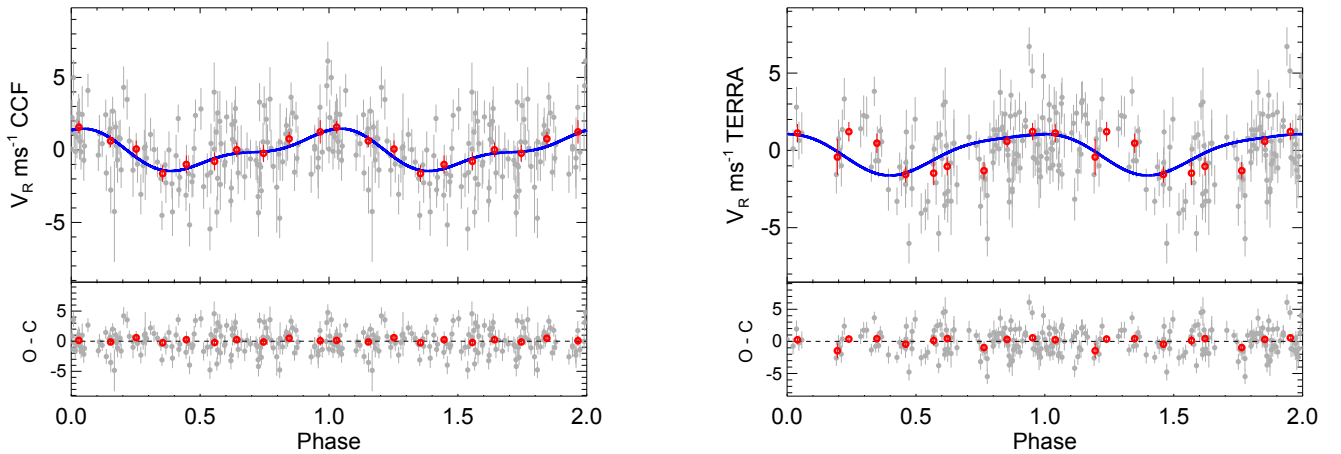


Fig. 7. Phase-folded curve of the RV data using the 74-day periodicity for the CCF data (*left panel*) and the 86-day periodicity for the TERRA data (*right panel*) after subtracting the signals shown in Fig. 6. The red dots are the same points binned in phase with a bin size of 0.1. The error bar of a given bin is estimated using the weighted standard deviation of binned measurements divided by the square root of the number of measurements included in this bin. The blue solid line shows the best fit to the data using a double harmonic sinusoidal fit.

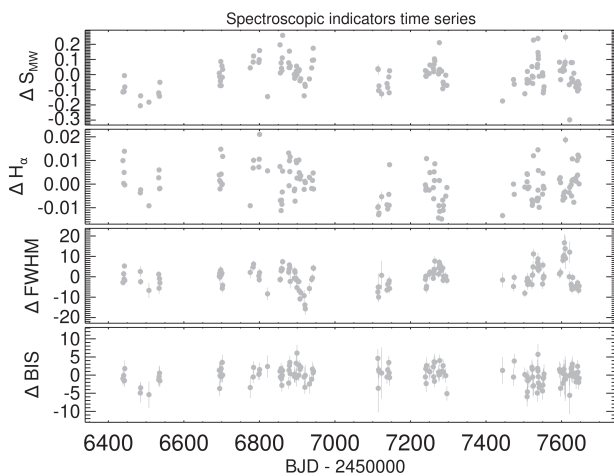


Fig. 8. Time series of the spectroscopic indicators. *From top to bottom:* S_{MW} index, H_{α} index, FWHM (in m s^{-1}), and bisector span (in m s^{-1}) time series.

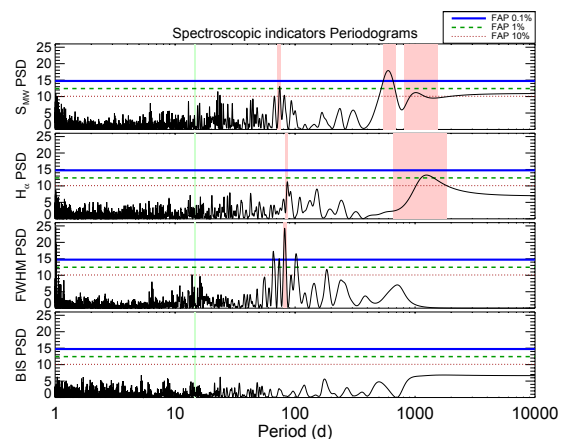


Fig. 9. Periodograms of the spectroscopic indicators. *From top to bottom:* S_{MW} index, H_{α} index, FWHM, and bisector span time series. The light red shaded regions show the detected periodicities. The light green shaded region shows the position of the 14.6 d signal detected in RV.

The 3.4 yr signal appears as a significant peak in the H_{α} index time series and as a less significant peak in the S_{MW} index time

series, indicating a probable common origin. This signal is probably the fingerprint of the magnetic cycle of the star. A 3.4 yr

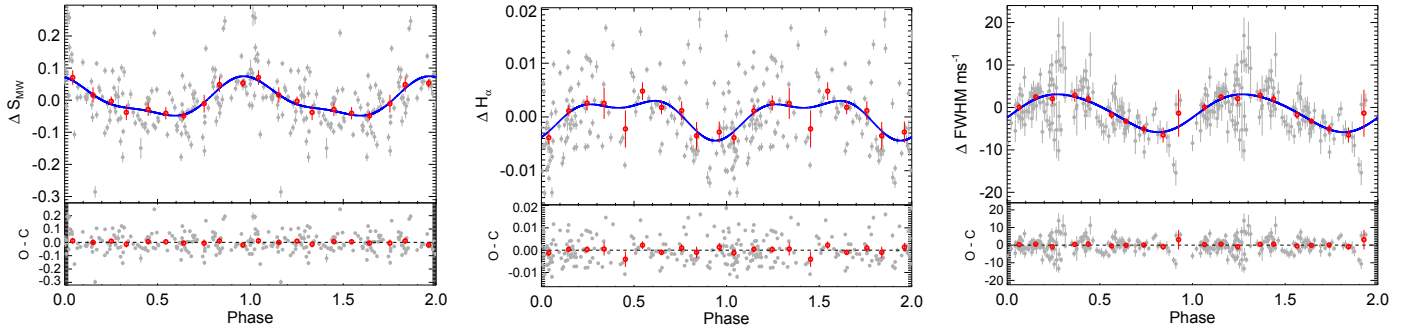


Fig. 10. Phase-folded curve for the S_{MW} index time series using the 74-day period, for the detrended H_α index time series using the 85-day period, and for the FWHM time series using the 82-day period. The grey dots are the individual measurements after subtracting the long-term variations. The red dots are the same points binned in phase with a bin size of 0.1. The error bar of a given bin is estimated using the weighted standard deviation of binned measurements divided by the square root of the number of measurements included in this bin. The blue solid line shows the best fit to the data using a double harmonic sinusoidal fit.

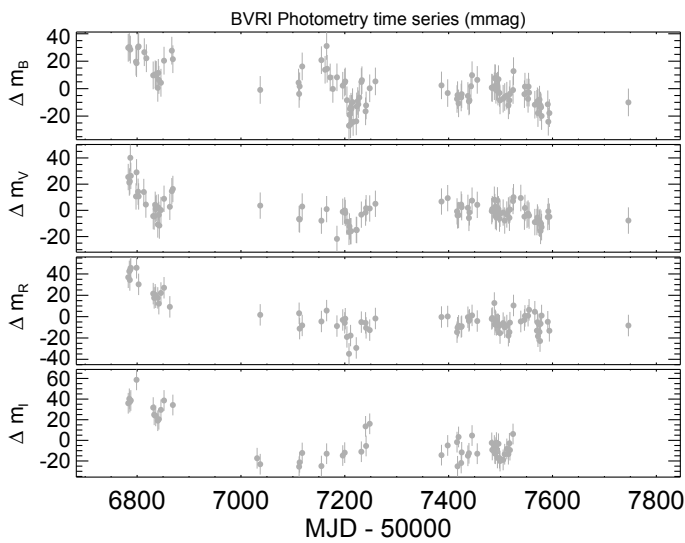


Fig. 11. Time series of the BVRI photometry. *From top to bottom:* m_B , m_V , m_R , and m_I time series.

cycle is shorter than expected for solar-type stars, but is in the range of previous measurements for M dwarfs (Robertson et al. 2013; Suárez Mascareño et al. 2016). The signal at 1.7 yr could have different interpretations. On the one hand, we could be seeing the first harmonic of the 3 yr signal due to the non-sinusoidal shape of the cycle (Waldmeier 1961; Baliunas et al. 1995). On the other hand, it could be a flip-flop cycle, i.e. a cycle of spatial rearrangement of active regions (Berdyugina & Usoskin 2003; Moss 2004). The short baseline of observations proves to be a problem for the correct interpretation of these signals. We could be measuring the global cycle and a flip-flop cycle, or the global cycle (3 yr) and its first harmonic, or even a flip-flop cycle and its first harmonic. At this stage, with our baseline being so close to the measured cycle length we cannot rule out the possibility of having an artefact of a poorly constrained long-term signal. Many years of data are probably needed before we can give a definitive answer.

The group of signals at 74, 82, and 85 days that appear in the different spectroscopic indicators, photometric series, and radial-velocity series, are probably related to the stellar rotation. Given the activity level of the star ($\log_{10}(R'_{HK}) = -5.5 \pm 0.2$) we expect the rotation period to be around 80 ± 20 days (Suárez Mascareño et al. 2015, 2016), and the semi-amplitude of the induced radial-velocity signal to be

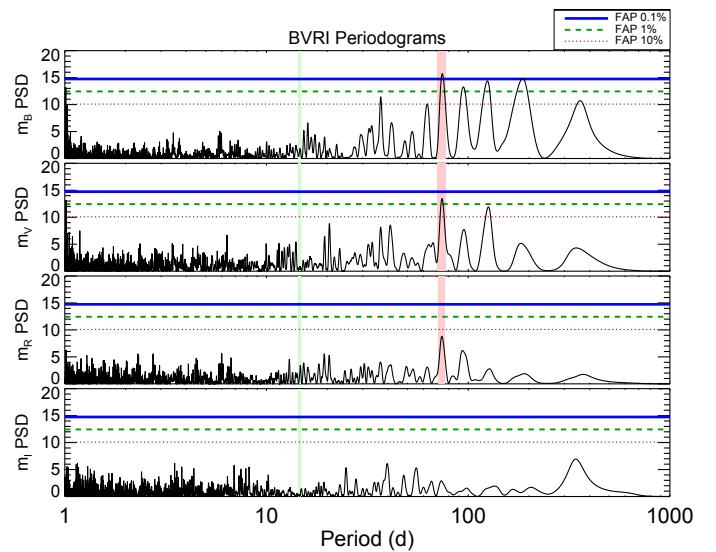


Fig. 12. Periodograms for the BVRI photometry. *From top to bottom:* m_B , m_V , m_R , and m_I periodograms. The light red shaded regions show the detected periodicities. The light green shaded region shows the position of the 14.6-day signal detected in RV.

$\sim 1.5 \text{ m s}^{-1}$ (Suárez Mascareño et al. 2017b). Scandariato et al. (2017) found a similar periodicity using a pooled variance analysis in the Ca II H&K and H_α fluxes, and the V-band photometric time series. The five signals around 74 days (RV, CCF, S_{MW} , m_B , m_V , and m_R) give us a strong indication of the stellar rotation, probably in a region close to the equator. The decline in amplitude when moving to redder bands in photometry might be an indication that we are measuring a modulation based on photospheric inhomogeneities, for which the contrast gets reduced when going to redder wavelengths. The signal at 85 days seen in the H_α index and RV TERRA time series probably shows the rotation period at higher latitudes, giving us a hint regarding the differential rotation of this star. Because the signal is only present in the H_α and RV variations, we are probably seeing a modulation based only on chromospheric inhomogeneities. The 82-day signal seen in the FWHM could be either a signal based on inhomogeneities in an intermediate latitude or an average of all the measured inhomogeneities along all latitudes. The two different RV induced signals for the two algorithms could imply that the two different RV algorithms are sensitive to the effect of different groups of inhomogeneities. While the CCF measurements seem

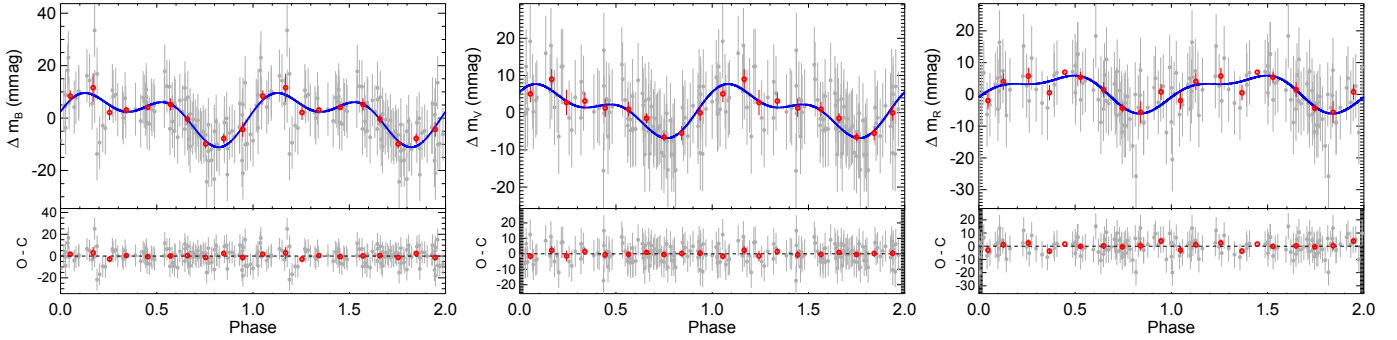


Fig. 13. Phase-folded curve of the data for the B , V , and R filter time series using the 74-day periodicity. The grey dots are the individual measurements after subtracting the long-term variations. The red dots are the same points binned in phase with a bin size of 0.1. The error bar of a given bin is estimated using the weighted standard deviation of binned measurements divided by the square root of the number of measurements included in this bin. The blue solid line shows the best fit to the data using a double harmonic sinusoidal fit.

Table 2. Available photometric measurements.

Band	N_{Obs}	T_{Span} (yr)	RMS (mmag)	σ (mmag)
B	108	2.6	13.6	10.1
V	98	2.6	10.4	10.0
R	82	2.6	16.5	10.0
I	55	2.0	21.1	10.0

to be in line with the photometric and Ca II H&K variations, the TERRA measurements appear coherent the H_{α} variations.

The signal at 14.6 days appears in both analyses of the RV time series with parameters that are consistent with each other. There is no evidence of signals at this period in any of the available activity proxies (see Table 3).

As a second test we measured the Spearman correlation coefficient between the S_{MW} , the H_{α} index, the FWHM, the bisector span, and the radial velocities. We do not find a strong correlation between any of these quantities and the raw radial velocities; the only significant correlation – especially for the CCF quantities – is between the FWHM and the RVs. All the correlation coefficients remain non-significant if we subtract the 74- and 85-day signals, isolating the 14.6-day signal (see Table 4). For the case of the FWHM vs. RV correlation, we see the coefficient going down significantly. When we subtract the 14.6 day signal, isolating the 74 day or 85 day signals, we see the RV vs. S_{MW} correlation coefficients going up and the RV vs. FWHM correlation coefficient recovering the raw value. This constitutes new evidence of the stellar origin of the 74 day and 85 day signals, and of the planetary origin of the 14.6 day signal. Although the correlation coefficients are not very high in any case, it seems clear that isolating the 14.6 day signal reduces the correlation between the different activity proxies and the RV measurements, while isolating the 74 day or 85 day signal does not, and even increases it for the S_{MW} .

Following this idea, we subtract the linear correlation between the radial velocity and the two activity diagnostic indexes that showed a significant correlation. When doing this we see that the strength of the 14.6 day signal remains constant, or even increases, while the significance of the 74 day and 85 day signals decrease slightly in all cases (see Fig. 14).

Keplerian signals are deterministic and consistent in time. When measuring one signal, we expect to find that the significance of the detection increases steadily with the number of observations, and that the measured period remains stable over time. However, in the case of activity related signal this is not necessarily the case. As the stellar surface is not static,

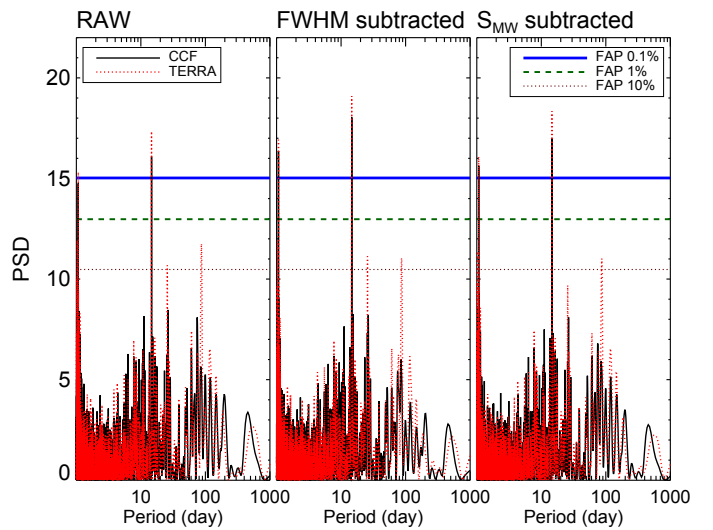


Fig. 14. Periodograms for the radial velocity after removing the correlation with the different activity diagnostic tools that showed a significant correlation coefficient. From left to right: periodogram for the original data, periodogram after detrending against the FWHM, and periodogram after detrending against the S_{MW} index.

and the configuration of active regions may change with time, changes in the phase of the modulation and in the detected period are expected (Affer et al. 2016; Suárez Mascareño et al. 2017a; Mortier & Collier Cameron 2017). Even the disappearance of the signal at certain seasons is possible. To study the evolution of both signals we perform a simultaneous fit of the detected periodicities in each of the time series, and then use the derived parameters to subtract the contribution of one of them leaving the other “isolated”. We then perform the stacked periodograms using a very narrow frequency window around each of the signals. Figure 15 shows the evolution of the PSD of the detection of both isolated signals. Once we gain a high enough signal-to-noise ratio, the 14.6 day signal increases steadily with the number of measurements. On the other hand the behaviour of the 74 day and 85 day signals is more erratic, especially for the case of the 85 day signal in the TERRA data. This is consistent with the attributed stellar origin, although we cannot rule out that the fluctuations are created by the lack of a sufficient signal-to-noise ratio for those signals.

Of the different significant radial-velocity signals detected in our data, it seems clear that the signal at 14.6 day has a planetary origin, while those at 74 day and 85 day have stellar activity origins.

Table 3. Detected signals in the different datasets of GJ 625.

Dataset	14.6 d	Amp	74 d	Amp	82 d	Amp
RV CCF	14.629 ± 0.069 d	1.85 ± 0.13 m s ⁻¹	74.7 ± 1.9 d	1.64 ± 0.18 m s ⁻¹		
RV TERRA	14.629 ± 0.077 d	1.65 ± 0.18 m s ⁻¹				
S_{MW}			73.7 ± 2.2 d	0.0413 ± 0.0020		
H_α						
FWHM					82.0 ± 3.1 d	4.03 ± 0.38 m s ⁻¹
m_B			73.9 ± 3.4 d	12.1 ± 0.3 mmag		
m_V			73.9 ± 3.7 d	8.2 ± 0.3 mmag		
m_R			73.6 ± 2.8 d	7.8 ± 0.3 mmag		
Dataset	85 d	Amp	1.7 yr	Amp	3.4 yr	Amp
RV CCF						
RV TERRA	85.9 ± 2.8 d	1.58 ± 0.18 m s ⁻¹				
S_{MW}			1.7 ± 0.2 yr	0.08162 ± 0.0024	3.2 ± 1.0 yr	0.05849 ± 0.0024
H_α	85.2 ± 2.2 d	0.00217 ± 0.00014			3.4 ± 1.6 yr	0.00593 ± 0.00017
FWHM						
m_B						
m_V						
m_R						

Notes. The parameters were calculated using least-squares minimization.

Table 4. Activity – radial-velocity correlations.

Parameter	Raw data	14.6 d signal	74 d signal	85 d signal
S_{MW} vs. V_R CCF	0.08 (1σ)	-0.05 ($<1\sigma$)	0.14 (2σ)	
S_{MW} vs. V_R TERRA	0.09 (1σ)	-0.01 ($<1\sigma$)		0.13 (2σ)
H_α vs. V_R CCF	-0.08 (1σ)	-0.08 (1σ)	0.02 ($<1\sigma$)	
H_α vs. V_R TERRA	0.01 ($<1\sigma$)	-0.03 ($<1\sigma$)		0.05 ($<1\sigma$)
FWHM vs. V_R CCF	0.23 (2σ)	0.14 (1σ)	0.22 (2σ)	
FWHM vs. V_R TERRA	0.15 (2σ)	0.06 ($<1\sigma$)		0.14 (2σ)
BIS vs. V_R CCF	0.04 ($<1\sigma$)	0.05 ($<1\sigma$)	0.06 ($<1\sigma$)	
BIS vs. V_R TERRA	-0.01 ($<1\sigma$)	0.01 ($<1\sigma$)		-0.01 ($<1\sigma$)

Notes. The value in parentheses indicates the significance of the correlation. The long-term variations of activity indicators have been subtracted.

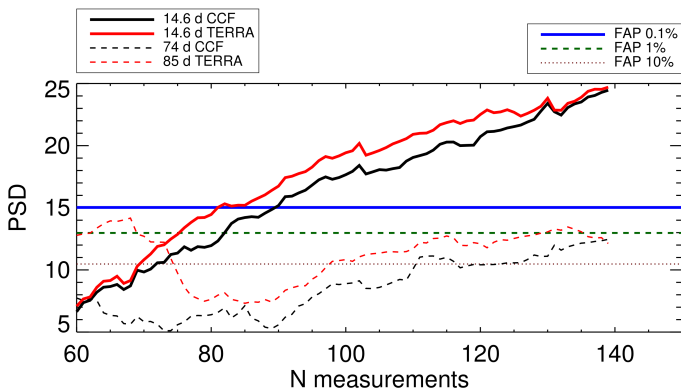


Fig. 15. Evolution of the significance of the detections for the isolated signals. The thick lines show the 14.6-day signal, dashed lines represent the 74-day and 85-day signals. The black lines represent the CCF signals, red lines the TERRA signals.

Finally, an analysis of the spectral window ruled out that the peak in the periodogram attributed to the Keplerian signal is an artefact of the time sampling. No features appear at 14.6 day,

even after masking the oversaturated regions of the power spectrum. The region around 70–90 days is more complicated in the HARPS-N spectral window, and casts some doubts on those periodicities, but that region is perfectly clean in the spectral window for the photometric time series. This suggests that the signals that we attributed to rotation in the RVs and spectroscopic indicators are real, but it also might explain the differences between the various indicators and the two different RV time series through spectral leakage of the real signal (Scargle 1982). We also recognize a prominent feature at 36.8 days, which should be treated with caution when searching for additional planets in the future. Figure 16 shows the spectral windows of the HARPS-N and photometric time series, along with a comparison between the RV periodogram around the 14.6 day signal and the spectral window in the same region. Following Rajpaul et al. (2016), we tried to re-create the 14.6-day signal by injecting the P_{Rot} signal along with a second signal at $P_{\text{Rot}}/2$ at 1000 randomized phase shifts with a white noise model. Additionally, we added a second set of signals at 3 yr and 1.5 yr to account for the possible effect of the magnetic cycle. We were not able to generate a signal at 14.6 days, or any significant signal at periods close to 14.6 days. It seems very unlikely that any of the signals are artefacts of the sampling. On the other hand, the process created many spurious

Table 5. MCMC parameters and uncertainties.

Parameter	TERRA			CCF			Prior
	Value	Upper error	Lower error	Value	Upper error	Lower error	
P_{planet} [d]	14.628	+0.012	-0.013	14.638	+0.012	-0.013	10.5–18.5
γ [m s ⁻¹ + 12 850]	-0.11	+0.18	-0.18	-0.07	+0.19	-0.20	-3.0+3.0
e	0.13	+0.12	-0.09	0.13	+0.13	-0.09	0.0–0.99
ω [deg]	343.1	+9.6	-14.8	240	+70	-180	0.0–360.0
χ	0.94+	+0.026	-0.043	0.26	+0.45	-0.18	0.0–0.99
K_{planet} [m s ⁻¹]	1.67	+0.29	-0.29	1.79	+0.29	-0.30	0.0–3.0
a [AU]	0.078361	+0.000044	-0.000046	0.078399	+0.000042	-0.000045	–
$m_p \sin i$ [M_{Earth}]	2.82	+0.51	-0.51	3.02	+0.49	-0.50	–
P_{Rot} [d]	84.7	+1.3	-1.8	76.1	+8.9	-3.0	65.0–95.0
K_{Rot} [m s ⁻¹]	1.41	+0.53	-0.47	1.25	+0.52	-0.39	0.0–3.0
RV noise [m s ⁻¹]	1.61	+0.18	-0.18	1.48	+0.18	-0.17	0.0–3.0

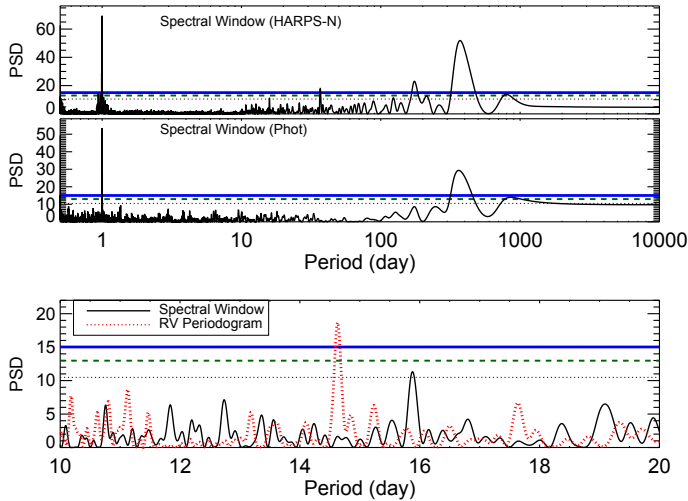


Fig. 16. Spectral windows for the HARPS data (*top panel*) and the photometric data (*middle panel*). *Bottom panel*: radial-velocity periodogram (red dotted line) compared to the spectral window (black solid line) in the range of periods around the signal for the planet candidate.

peaks at periods between 35 and 120 days. Future observations should take into account the possibility of having aliases and artefacts of the rotation arising in a wide range of periodicities.

6. MCMC modelling of the GJ 625 b planet

The analysis of the radial-velocity time series and of the activity indicators leads us to conclude that the best explanation of the observed data is the existence of a planet orbiting the star GJ 625 at the period of 14.6 day. The best solution comes from a super-Earth with a minimum mass of $2.8 M_{\oplus}$ orbiting at 0.078 AU from its star.

In order to quantify the uncertainties of the orbital parameters of the planet, we perform a Bayesian analysis using the code EXOFIT (Balan & Lahav 2009) as outlined in Suárez Mascareño et al. (2017a). This code follows the Bayesian method described in Gregory (2005), Ford (2005) and Ford & Gregory (2007). A single planet can be modelled using the formula

$$v_i = \gamma - K[\sin(\theta(t_i + \chi P) + \omega) + e \sin \omega], \quad (3)$$

where γ is the system's radial velocity; K is the semi-amplitude of the velocity, equal to $2\pi P^{-1}(1 - e^2)^{-1/2}a \sin i$; P is the orbital period; a is the semi-major axis of the orbit; e is the orbital eccentricity; i is the inclination of the orbit; ω is the longitude of periastron; χ is the fraction of an orbit, prior to the start of data taking, at which periastron occurs (thus, χP equals the number of days prior to $t_i = 0$ that the star was at periastron, for an orbital period of P days); and $\theta(t_i + \chi P)$ is the angle of the star in its orbit relative to periastron at time t_i , also called the true anomaly.

To fit the previous equation to the data we need to specify the six model parameters: P , K , γ , e , ω , and χ . Observed radial-velocity data, d_i , can be modelled by the equation $d_i = v_i + \epsilon_i + \delta$ (Gregory 2005), where v_i is the calculated radial velocity of the star and ϵ_i is the uncertainty component arising from accountable but unequal measurement errors, which are assumed to be normally distributed. The term δ contains any unknown measurement error. Any noise component that cannot be modelled is described by the term δ . The probability distribution of δ is chosen to be a Gaussian distribution with finite variance s^2 . Therefore, the combination of uncertainties $\epsilon_i + \delta$ has a Gaussian distribution with a variance equal to $\sigma_i^2 + s^2$ (see Balan & Lahav 2009, for more details).

In Table 5 we show the final parameters and uncertainties obtained with the MCMC Bayesian analysis with the code EXOFIT. We performed a simultaneous fit of the planetary signal and the activity-induced signal using both the CCF and the TERRA data. The obtained parameters are compatible in both datasets, except

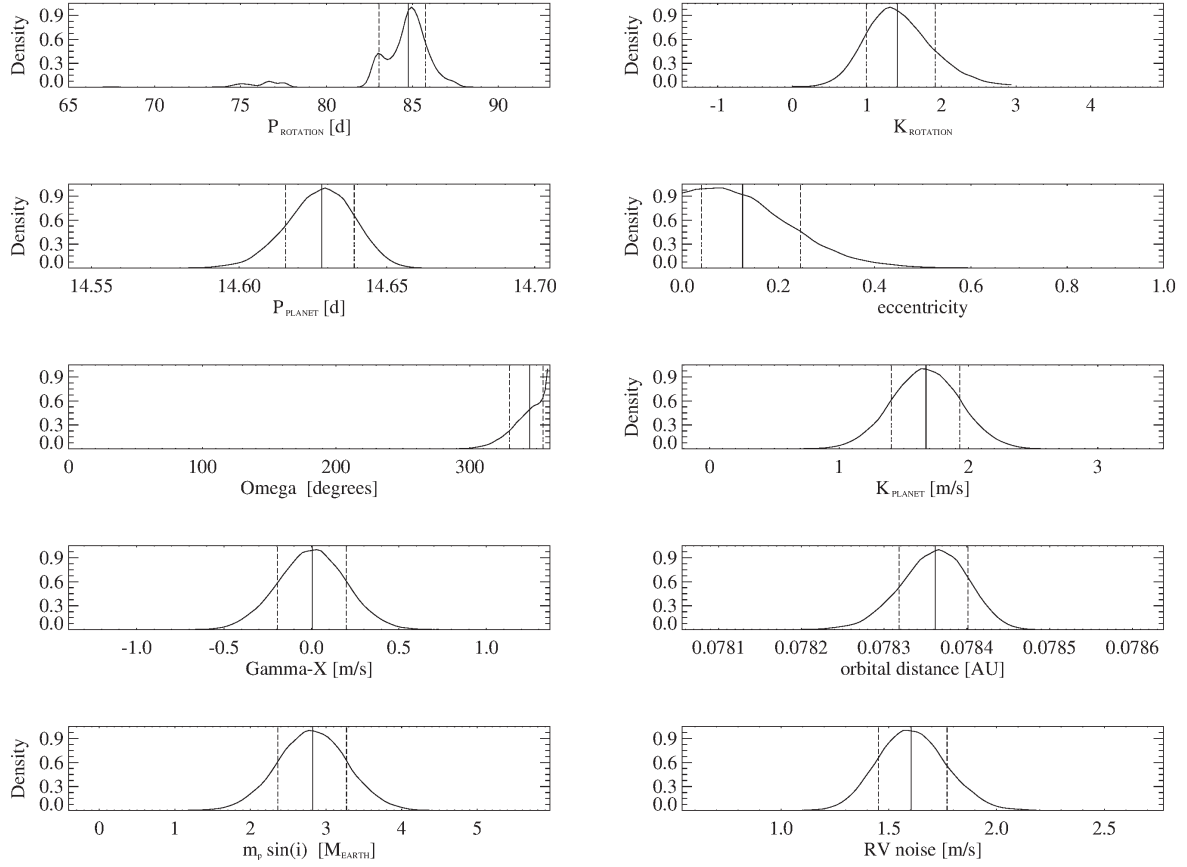


Fig. 17. Posterior distribution of model parameters of the planet companion of the M-dwarf star GJ 625 using the RV measurements given by the TERRA pipeline. Vertical dashed line show the median value of the distribution and the dotted lines the 1σ values.

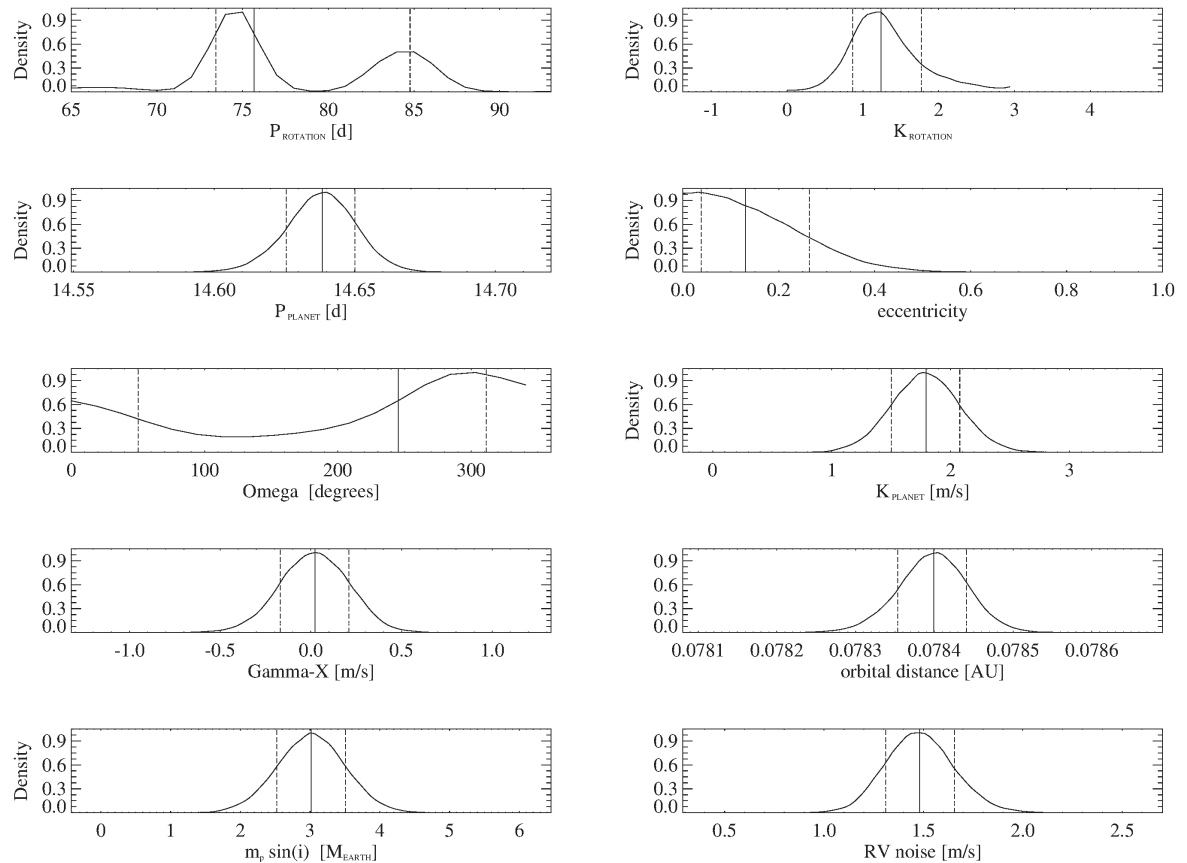


Fig. 18. Posterior distribution of model parameters of the planet companion of the M-dwarf star GJ 625 using the RV measurements given by the CCFs. Vertical dashed line show the median value of the distribution and the dotted lines the 1σ values.

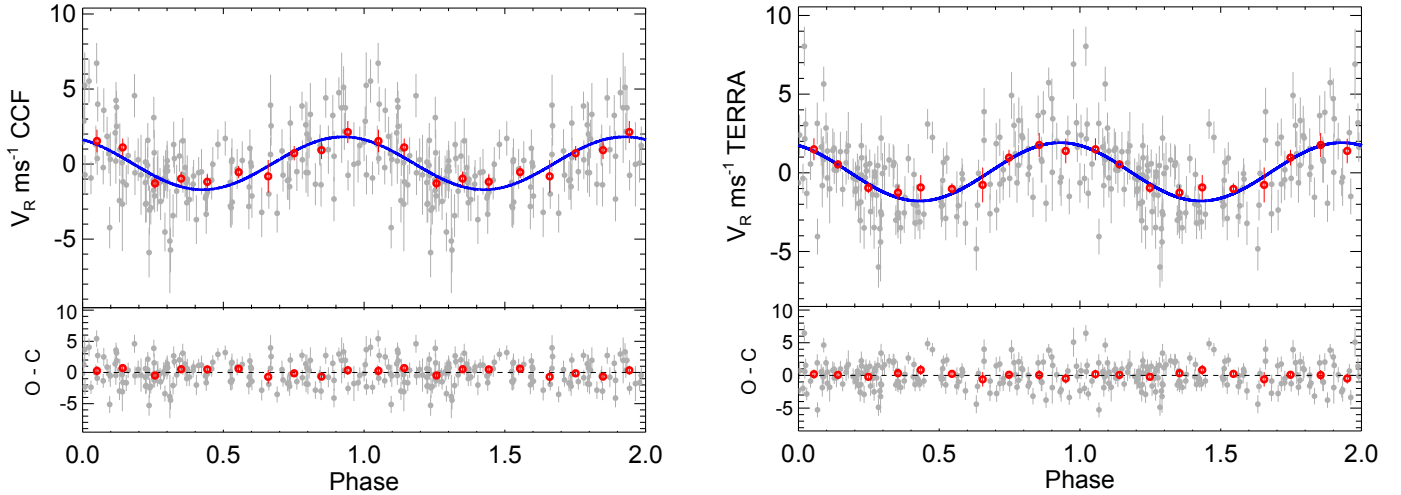


Fig. 19. Phase-folded curve of the planetary signal detected in GJ 625 using the parameters of the MCMC model. *Left panel:* CCF measurements, *Right panel:* TERRA measurements. The grey dots show the measurements after subtracting the detected activity-induced signals. The red dots are the same points binned in phase with a bin size of 0.1. The error bar of a given bin is estimated using the weighted standard deviation of binned measurements divided by the square root of the number of measurements included in this bin. The blue line shows the best fit to the data using a Keplerian model.

for ω and χ . However, in those cases the uncertainties are large, suggesting that more data might be needed to better define the solution. Figures 17 and 18 show the probability densities for all the parameters in both situations and Fig. 19 shows the best fit to the data obtained for the RV signal attributed to the planet candidate GJ 625 b. The TERRA data gives a smaller RV amplitude and smaller mass and a smaller RMS of the residuals. The noise factor in both cases exceeds the typical uncertainties of our data, indicating the presence of unaccounted signals in the radial-velocity data. The smaller RMS of the residuals after the fit of the TERRA data – even though they show a higher RV noise factor – and the tighter parameter results lead us to favour the model given by the TERRA data. The RMS of the remaining residuals is 1.8 m s^{-1} , smaller than the HADES noise contribution estimated in [Perger et al. \(2017a\)](#).

7. Discussion

We detect a planet with a semi-amplitude of 1.6 m s^{-1} ; given the stellar mass of $0.3 M_{\odot}$, this converts to $m_p \sin i$ of $2.75 M_{\oplus}$, orbiting with a period of 14.6 d around GJ 625, an M2-type star with a mean rotation period of around 78 day and an additional activity signal compatible with an activity cycle of around 3 yr. We have seen hints of differential rotation, with the difference between the shortest and the longest period going up to 11 days.

The planet is a small super-Earth at the edge of the habitable zone of its star. Using a basic estimation of the equilibrium temperature, and a correction using the greenhouse calculated to estimate the surface temperature, we estimate a mean surface temperature of 350 K for a Bond albedo $A = 0.3$ and Earth-like greenhouse effect. Surface temperatures close to earth surface temperature can be reached for many combinations of albedo and greenhouse effect. Following [Kasting et al. \(1993\)](#) and [Selsis et al. \(2007\)](#), we perform a simple estimation of the habitable zone (HZ) of this star. The HZ would go from 0.099 to 0.222 AU in the narrowest case (cloud free model), and from 0.057 to 0.305 AU in the broader case (fully clouded model). Figure 20 shows the distribution of surface mean temperatures for the different combination of bond albedo and greenhouse levels and the evolution of the habitable zone following [Selsis et al. \(2007\)](#). The estimation of the habitable zone

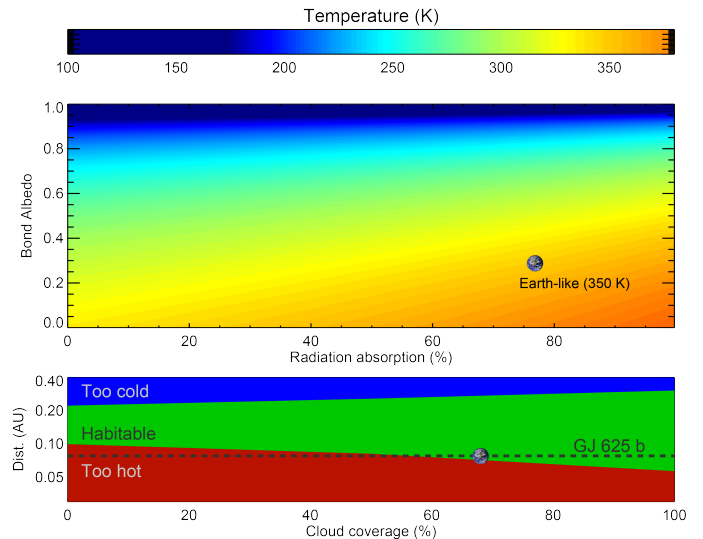


Fig. 20. Mean surface temperature of GJ 625 b as a function of albedo and the fraction of radiation absorbed by the atmosphere (*top panel*) and change of the habitable zone as a function of cloud coverage of the planet (*bottom panel*). The Earth symbol shows where it would be with an Earth-like albedo and greenhouse effect (*top panel*), and with an Earth-like cloud coverage (*bottom panel*).

performed by [Kopparapu \(2013\)](#) for a cloud-free model would leave the most optimistic inner limit of the HZ at 0.088 AU. If we assume that the HZ evolves with the cloud coverage of the atmosphere of the planet in the same way as in [Selsis et al. \(2007\)](#), then the most optimistic limit of the inner HZ would move down to 0.043 AU for a completely covered atmosphere, following almost exactly the same pattern as in [Selsis et al. \(2007\)](#). We find that GJ 625 b might potentially host liquid water, depending on its atmospheric conditions.

The habitability of planets in close orbits around low mass stars is currently a subject of debate. Planets are probably tidally locked and exposed to the strong magnetic field, flares, and UV and X-ray irradiation of their parent stars. But even if these are strong arguments against their habitability, none of

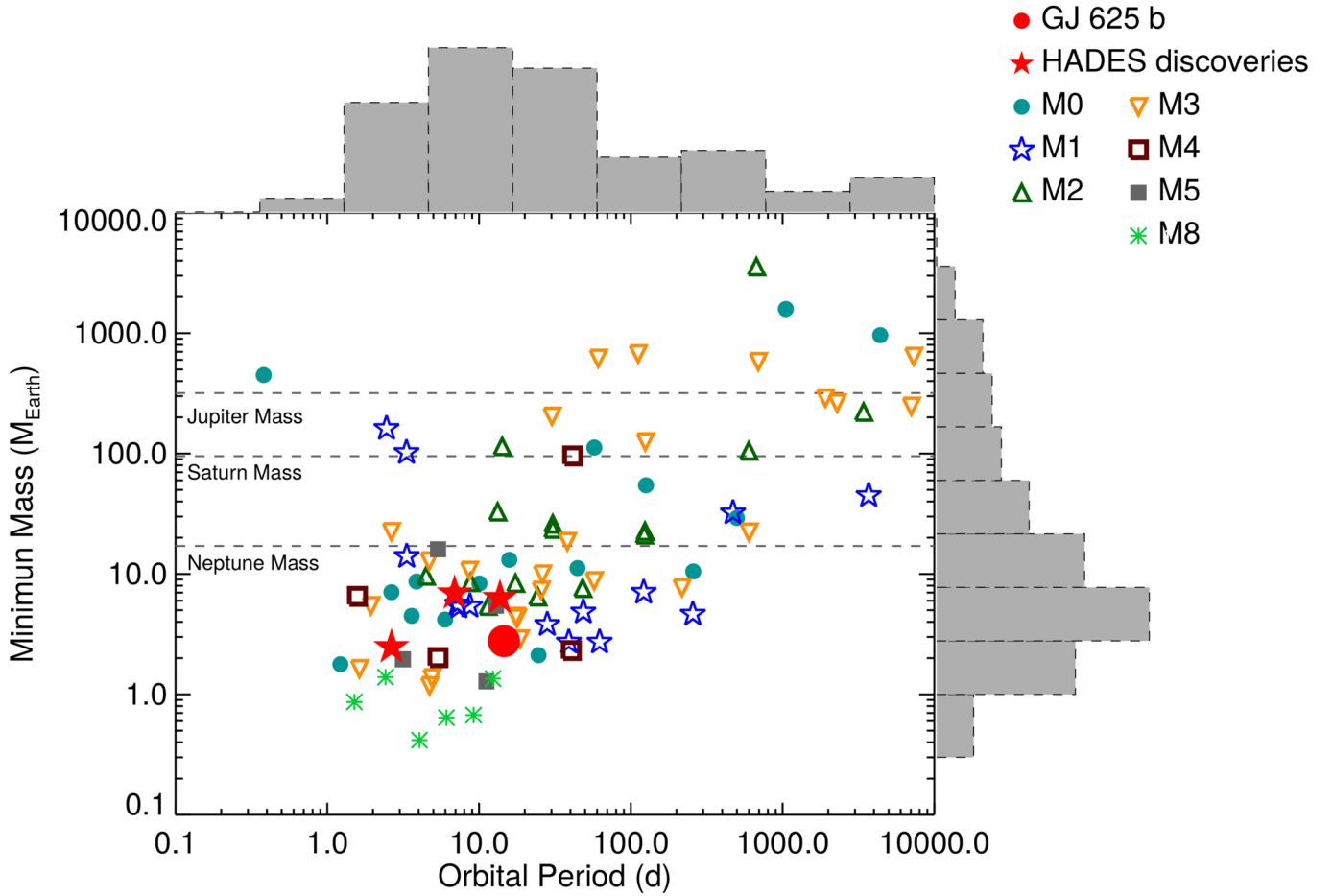


Fig. 21. Minimum mass vs. orbital period for the known planets with determined masses around M-dwarf stars (using data from exoplanet.eu) divided by the spectral type of the host star. The red filled dot shows the position of GJ 625 b, and the red filled stars show the position of GJ 3998 b, c and GJ 3942 b (Affer et al. 2016; Perger et al. 2017b). The horizontal dashed lines show the mass of the solar system planets for comparison. The distribution for each parameter is shown at the edges of the figure.

them is definitive. Depending on the planet’s composition and its own magnetic field, it might be able to prevent all but a small atmospheric loss (Vidotto et al. 2013; Zuluaga et al. 2013; Anglada-Escudé et al. 2016; Ribas et al. 2016; Bolmont et al. 2017).

GJ 625 b is in the lower part of the mass vs. period diagram of known planets around M-dwarf stars with measured dynamic masses (Fig. 21). The proposed projected mass would make it the lightest planet found around an M2 star to date. Of all the known planets around M dwarfs with dynamical masses determined $\sim 52\%$ are super-Earths or Earth-like planets ($< 10 M_{\oplus}$) at periods shorter than 100 days. Figure 21 shows once more the lack of massive planets in close orbits around M dwarfs, only $\sim 9\%$ of the detected planets at periods shorter than 10 days are heavier than $10 M_{\oplus}$ and only one goes over $1 M_{Jup}$, as expected by the core-accretion formation model (Laughlin et al. 2004). There is also a lack of small planets ($< 3 M_{\oplus}$) in close orbits (< 10 days) around early M dwarfs (M0-M2); GJ 3998 is the only one. At periods longer than 10 days, on the other hand, there is a great abundance of planets with these characteristics.

The presence of one or more extra planets around the star GJ 625 cannot yet be ruled out at longer orbital periods and small RV amplitudes ($< 1.5 \text{ m s}^{-1}$ for periods shorter than 3 yr), but finding them will not be easy. The rotation period, combined with the signs of differential rotation, would make the detection of low amplitude planetary signals difficult in the range

of periods from 35 to 120 days, as stated at the end of Sect. 5. Also, considering the detected magnetic cycle we would eventually expect to find a RV signal arising at 1.5 yr or 3 yr. The most promising candidates to continue searching would be very small mass planets at very close orbits, and small mass planets in the habitable zone of the star, at periods shorter than 30 days.

The activity-induced RV variations measured using the CCF fitting and using the TERRA pipeline are not consistent with each other. With the CCF fitting favouring a signal at 74 days, very similar to the ones measured in the B -, V -, and R -band photometry, and in the Ca II H&K variations, while the TERRA pipeline favours an 85 day signal closest to the signal measured in the H_{α} index. Stellar induced signals are usually more complicated than planetary signals, and the long period and low amplitude of the signals ($\sim 1.6 \text{ m s}^{-1}$), combined with their non-sinusoidal shape, could easily lead to an incorrect model. The spectral window of the observation series might also be playing a part here. The region around 70–100 days is a complicated one, so it cannot be ruled out that it is affecting the 82- and 85-day measurements. If we assume that this is not the case, it could be that the change in the source of RV information (a selection of lines in the CCF vs. the full spectrum in TERRA) is making the two algorithms sensitive to different active regions or even different depths of the stellar atmosphere. If this were the case, using both algorithms for the same star could prove a very useful tool for the diagnosis of activity-induced signals, maybe even for

the case of earlier spectral types (G- and K-type stars). Further investigation using data from different stars would be needed.

GJ 625 has an estimated mass of $0.3 M_{\odot}$, placing it close to the theoretical limit at which a star becomes fully convective. If the proposed 3 yr magnetic cycle could be confirmed it would place GJ 625 in the small group of very low mass stars which exhibit activity cycles despite theoretical predictions suggesting they should not (Chabrier & Küker 2006; Robertson et al. 2014; Suárez Mascareño et al. 2016; Wargelin et al. 2017). The growing number of detected cycles in stars that are expected to be fully convective, and therefore without a tachocline, supports the idea that the stellar dynamo might not be confined to the tachocline, but instead that it is distributed across the convection zone (Wright et al. 2016).

8. Conclusions

We have analysed 151 high resolution spectra along with photometric observations in four different bands to study the presence of planetary companions around the M-dwarf star GJ 625 and its stellar activity. For the study of this system, we extracted the information regarding radial velocity in two different ways, by using the cross-correlation of the spectra with a numerical template and by template matching the individual spectra with a high S/N template.

We detected one significant radial-velocity signal at a period of 14.6 day. A second signal arises at 74–85 days, with different periods for the different algorithms. From the available photometric and spectroscopic information we conclude that the 14.6 day signal is caused by a planet with a minimum mass of $2.82 M_{\oplus}$ in an orbit with a semi-major axis of 0.078 AU. The planet is on the inner edge of the habitable zone and its mean surface temperature is very dependent on the atmospheric parameters. The short period of the planet makes it a potential transiting candidate. Following Winn (2010) we find the transit probability of GJ 625 b in the range of 1.5–2.5%. Detecting the transits would give a new constraining point to the mass-radius diagram and provide further opportunity for atmospheric characterization.

The second radial-velocity signal of period 74–85 day and semi-amplitude of 1.6 m s^{-1} is a magnetic activity-induced signal related to the rotation of the star. Using the photometric light curves and the time series of spectral indicators we conclude that the rotation period of the star is ~ 74 days; there is evidence of differential rotation of up to ~ 85 days. We have seen that the measured rotation period and the amplitude of the rotation induced signal match the expected results of Suárez Mascareño et al. (2015, 2016, 2017b). We also found evidence of a magnetic cycle of ~ 3 yr, which would need future observations to be better constrained.

Acknowledgements. We thank Guillem Anglada-Escudé for distributing the latest version of the TERRA pipeline. This research has made extensive use of the SIMBAD database, operated at CDS, Strasbourg (France), and NASA's Astrophysics Data System. This work has been financed by the Spanish Ministry project MINECO AYA2014-56359-P. J.I.G.H. acknowledges financial support from the Spanish MINECO under the 2013 Ramón y Cajal programme MINECO RYC-2013-14875. A.S.M. acknowledges financial support from the Swiss National Science Foundation (SNSF). M.P., I.R., J.C.M., E.H., A.R., and M.L. acknowledge support from the Spanish Ministry of Economy and Competitiveness (MINECO) and the Fondo Europeo de Desarrollo Regional (FEDER) through grant ESP2016-80435-C2-1-R. GAPS acknowledges support from INAF through the "Progetti Premiali" funding scheme of the Italian Ministry of Education, University, and Research and through the PREMIALE WOW 2013 research project. L.A. and G.M. acknowledge support from the Ariel ASI-INAF agreement No. 2015-038-R.0. The research leading to these results has received funding from the European Union Seventh Framework Programme (FP7/2007–2013)

under Grant Agreement No. 313014 (ETAEARTH). G.S. acknowledges financial support from "Accordo ASI-INAF" No. 2013-016-R.0 July 9, 2013.

References

- Affer, L., Micela, G., Damasso, M., et al. 2016, *A&A*, **593**, A117
 Anglada-Escudé, G., & Butler, R. P. 2012, *ApJS*, **200**, 15
 Anglada-Escudé, G., Amado, P. J., Barnes, J., et al. 2016, *Nature*, **536**, 437
 Astudillo-Defru, N., Bonfils, X., Delfosse, X., et al. 2015, *A&A*, **575**, A119
 Astudillo-Defru, N., Forveille, T., Bonfils, X., et al. 2017, *A&A*, **602**, A88
 Balan, S. T., & Lahav, O. 2009, *MNRAS*, **394**, 1936
 Baliunas, S. L., Donahue, R. A., Soon, W. H., et al. 1995, *ApJ*, **438**, 269
 Baranne, A., Queloz, D., Mayor, M., et al. 1996, *A&AS*, **119**, 373
 Berdyugina, S. V., & Järvinen, S. P. 2005, *Astron. Nachr.*, **326**, 283
 Berdyugina, S. V., & Usoskin, I. G. 2003, *A&A*, **405**, 1121
 Berta-Thompson, Z. K., Irwin, J., Charbonneau, D., et al. 2015, *Nature*, **527**, 204
 Boisse, I., Bouchy, F., Hébrard, G., et al. 2011, *A&A*, **528**, A4
 Bolmont, E., Selsis, F., Owen, J. E., et al. 2017, *MNRAS*, **464**, 3728
 Bonfils, X., Mayor, M., Delfosse, X., et al. 2007, *A&A*, **474**, 293
 Bonfils, X., Delfosse, X., Udry, S., et al. 2013, *A&A*, **549**, A109
 Chabrier, G., & Küker, M. 2006, *A&A*, **446**, 1027
 Cosentino, R., Lovis, C., Pepe, F., et al. 2012, in *Ground-based and Airborne Instrumentation for Astronomy IV*, *SPIE*, **8446**, 8446I
 Covino, E., Esposito, M., Barbieri, M., et al. 2013, *A&A*, **554**, A28
 Cumming, A. 2004, *MNRAS*, **354**, 1165
 Delfosse, X., Bonfils, X., Forveille, T., et al. 2013, *A&A*, **553**, A8
 Dressing, C. D., & Charbonneau, D. 2013, *ApJ*, **767**, 95
 Dressing, C. D., Charbonneau, D., & Newton, E. R. 2015, in *AAS/Division for Extreme Solar Systems Abstracts*, **3**, 501.03
 Endl, M., Kürster, M., Els, S., Hatzes, A. P., & Cochran, W. D. 2001, *A&A*, **374**, 675
 Endl, M., Cochran, W. D., Kürster, M., et al. 2006, *ApJ*, **649**, 436
 Ford, E. B. 2005, *AJ*, **129**, 1706
 Ford, E. B., & Gregory, P. C. 2007, in *Statistical Challenges in Modern Astronomy IV*, eds. G. J. Babu, & E. D. Feigelson, *ASP Conf. Ser.*, **371**, 189
 Gaia Collaboration (Brown, A. G. A., et al.) 2016, *A&A*, **595**, A2
 Gaidos, E. 2013, *ApJ*, **770**, 90
 Gillon, M., Triaud, A. H. M. J., Demory, B.-O., et al. 2017, *Nature*, **542**, 456
 Gomes da Silva, J., Santos, N. C., Bonfils, X., et al. 2011, *A&A*, **534**, A30
 Gregory, P. C. 2005, *ApJ*, **631**, 1198
 Høg, E., Fabricius, C., Makarov, V. V., et al. 2000, *A&A*, **355**, L27
 Horne, J. H., & Baliunas, S. L. 1986, *ApJ*, **302**, 757
 Howard, A. W., Johnson, J. A., Marcy, G. W., et al. 2009, *ApJ*, **696**, 75
 Howard, A. W., Marcy, G. W., Bryson, S. T., et al. 2012, *ApJS*, **201**, 15
 Howard, A. W., Marcy, G. W., Fischer, D. A., et al. 2014, *ApJ*, **794**, 51
 Irwin, J., Berta-Thompson, Z. K., Charbonneau, D., Dittmann, J., & Newton, E. R. 2015, in *AAS Meeting Abstracts*, **225**, 258.01
 Jehin, E., Gillon, M., Lederer, S. M., et al. 2016, in *AAS/Division for Planetary Sciences Meeting Abstracts*, **48**, 302.07
 Kasting, J. F., Whitmire, D. P., & Reynolds, R. T. 1993, *ICARUS*, **101**, 108
 Kopparapu, R. K. 2013, *ApJ*, **767**, L8
 Labadie, L., Rebolo, R., Villó, I., et al. 2011, *A&A*, **526**, A144
 Laughlin, G., Bodenheimer, P., & Adams, F. C. 2004, *ApJ*, **612**, L73
 Lovis, C., Dumusque, X., Santos, N. C., et al. 2011, *ArXiv e-prints* [[arXiv:1107.5325](https://arxiv.org/abs/1107.5325)]
 Maldonado, J., Scandariato, G., Stelzer, B., et al. 2017, *A&A*, **598**, A27
 Markwardt, C. B. 2009, in *Astronomical Data Analysis Software and Systems XVIII*, eds. D. A. Bohlender, D. Durand, & P. Dowler, *ASP Conf. Ser.*, **411**, 251
 Mayor, M., Bonfils, X., Forveille, T., et al. 2009, *A&A*, **507**, 487
 Mayor, M., Marmier, M., Lovis, C., et al. 2011, *ArXiv e-prints* [[arXiv:1109.2497](https://arxiv.org/abs/1109.2497)]
 Montet, B. T., Crepp, J. R., Johnson, J. A., Howard, A. W., & Marcy, G. W. 2014, *ApJ*, **781**, 28
 Mortier, A., & Collier Cameron, A. 2017, *A&A*, **601**, A110
 Moss, D. 2004, *MNRAS*, **352**, L17
 Newton, E. R., Irwin, J., Charbonneau, D., Berta-Thompson, Z. K., & Dittmann, J. A. 2016, *ApJ*, **821**, L19
 Noyes, R. W., Hartmann, L. W., Baliunas, S. L., Duncan, D. K., & Vaughan, A. H. 1984, *ApJ*, **279**, 763
 Oscoz, A., Rebolo, R., López, R., et al. 2008, in *Ground-based and Airborne Instrumentation for Astronomy II*, *Proc. SPIE*, **7014**, 701447
 Pepe, F., Mayor, M., Delabre, B., et al. 2000, in *Optical and IR Telescope Instrumentation and Detectors*, eds. M. Iye, & A. F. Moorwood, *SPIE*, **4008**, 582

- Perger, M., García-Piquer, A., Ribas, I., et al. 2017a, *A&A*, **598**, A26
- Perger, M., Ribas, I., Damasso, M., et al. 2017b, *A&A*, submitted
- Poretti, E., Boccato, C., Claudi, R., et al. 2016, *Mem. Soc. Astron. It.*, **87**, 141
- Queloz, D., Henry, G. W., Sivan, J. P., et al. 2001, *A&A*, **379**, 279
- Quirrenbach, A., Amado, P. J., Seifert, W., et al. 2012, in *Ground-based and Airborne Instrumentation for Astronomy IV*, *Proc. SPIE*, **8446**, 84460
- Rajpaul, V., Aigrain, S., & Roberts, S. 2016, *MNRAS*, **456**, L6
- Reiners, A. 2009, *A&A*, **498**, 853
- Ribas, I., Bolmont, E., Selsis, F., et al. 2016, *A&A*, **596**, A111
- Robertson, P., Endl, M., Cochran, W. D., & Dodson-Robinson, S. E. 2013, *ApJ*, **764**, 3
- Robertson, P., Mahadevan, S., Endl, M., & Roy, A. 2014, *Science*, **345**, 440
- Saar, S. H., & Donahue, R. A. 1997, *ApJ*, **485**, 319
- Scandariato, G., Maldonado, J., Affer, L., et al. 2017, *A&A*, **598**, A28
- Scargle, J. D. 1982, *ApJ*, **263**, 835
- Selsis, F., Kasting, J. F., Levrard, B., et al. 2007, *A&A*, **476**, 1373
- Suárez Mascareño, A., Rebolo, R., González Hernández, J. I., & Esposito, M. 2015, *MNRAS*, **452**, 2745
- Suárez Mascareño, A., Rebolo, R., & González Hernández, J. I. 2016, *A&A*, **595**, A12
- Suárez Mascareño, A., González Hernández, J. I., Rebolo, R., et al. 2017a, *A&A*, **597**, A108
- Suárez Mascareño, A., Rebolo, R., González Hernández, J. I., & Esposito, M. 2017b, *MNRAS*, **468**, 4772
- Udry, S., Bonfils, X., Delfosse, X., et al. 2007, *A&A*, **469**, L43
- van Leeuwen, F. 2007, *A&A*, **474**, 653
- Vanderburg, A., Plavchan, P., Johnson, J. A., et al. 2016, *MNRAS*, **459**, 3565
- Velasco, S., Rebolo, R., Oscoz, A., et al. 2016, *MNRAS*, **460**, 3519
- Vidotto, A. A., Jardine, M., Morin, J., et al. 2013, *A&A*, **557**, A67
- Waldmeier, M. 1961, *The sunspot-activity in the years 1610–1960* (Zurich: Schulthess)
- Wargelin, B. J., Saar, S. H., Pojmański, G., Drake, J. J., & Kashyap, V. L. 2017, *MNRAS*, **464**, 3281
- Wildi, F., Pepe, F., Chazelas, B., Lo Curto, G., & Lovis, C. 2010, in *Ground-based and Airborne Instrumentation for Astronomy III*, *SPIE*, **7735**, 77354
- Winn, J. N. 2010, ArXiv e-prints [[arXiv:1001.2010](https://arxiv.org/abs/1001.2010)]
- Wright, D. J., Wittenmyer, R. A., Tinney, C. G., Bentley, J. S., & Zhao, J. 2016, *ApJ*, **817**, L20
- Zechmeister, M., & Kürster, M. 2009, *A&A*, **496**, 577
- Zuluaga, J. I., Bustamante, S., Cuartas, P. A., & Hoyos, J. H. 2013, *ApJ*, **770**, 23